An Investigation of MR Sequences for Partial Volume Correction in PET Image Reconstruction

by

Gong Wang

Medical Physics Program
Duke Kunshan and Duke University

Date: _____

Approved:

_____
James E. Bowsher, Supervisor

_____
Xin Chen

_____
Trong-Kha Truong

Thesis submitted in partial fulfillment of
the requirements for the degree of
Master of Science in the Department of
Medical Physics in the Graduate School
of Duke Kunshan and Duke University

2019

ABSTRACT

An Investigation of MR Sequences for Partial Volume Correction in PET Image Reconstruction

by

Gong Wang

Medical Physics
Duke Kunshan and Duke University

Date: _____

Approved:

_____
James E. Bowsher, Supervisor

_____
Xin Chen

_____
Trong-Kha Truong

An abstract of a thesis submitted in partial fulfillment of the requirements for the degree of Master of Science in the Department of Medical Physics in the Graduate School of Duke Kunshan and Duke University

2019

Abstract

Brain Positron emission tomography (PET) has been widely employed for the clinic diagnosis of Alzheimer's disease (AD). Studies have shown that PET imaging is helpful in differentiating healthy elderly individuals, mild cognitive impairment (MCI) individuals, and AD individuals (Nordberg, Rinne, Kadir, & Långström, 2010). However, PET image quality and quantitative accuracy is degraded from partial volume effects (PVEs), which are due to the poor spatial resolution of PET. As a result, the compensation of PVEs in PET may be of great significance in the improvement of early diagnosis of AD. There are many different approaches available to address PVEs including region-based methods and voxel-based methods. In this study, a voxel-based PVE compensation technique using high-resolution anatomical images was investigated. The high-resolution anatomical images could be computed tomography (CT) or magnetic resonance imaging (MRI) images. Such methods have been proposed and investigated in many studies (Vunckx et al., 2012). However, relatively little research has been done on comparing the effects of different MRI images on voxel-based PVE correction methods. In this study, we compare the effect of 6 different MRI image protocols on PVE compensation in PET images. The MRI protocols compared in this study are T1-, T2-, proton-density (PD)-weighted and 3 different inversion recovery MRI protocols.

Results: OSEM and MAP/ICD images with isotropic prior are blurry and/or noisy. Compared with the OSEM and MAP/ICD images obtained by using an isotropic

prior, the PET image reconstructed using anatomical information show better contrast and less noise. Visually, the PET image reconstructed with the ZeroCSF prior gave the PET image that visually appears to match best with the PET phantom. PET images reconstructed with T2, PD and ZeroWM image are similar to one another in image quality, but relative to the PET phantom and the ZeroCSF PET image, these images have poor contrast between CSF pockets and surrounding GM tissue, and they have less contrast between GM and WM. PET image reconstructed with T1 image had a better GM and CSF contrast, some of the CSF pockets in GM were reconstructed, but the WM region was very noisy. PET images reconstructed with ZeroGM image had noticeably worse performance on the GM reconstruction. Analysis suggest that these effects are caused by differences in tissue contrast with different MRI protocols

Keywords: PET, MRI, partial volume effect, image reconstruction, SPECT, Alzheimer's disease.

Contents

List of Tables

List of Figures

1. Introduction

1.1 The function of PET and MRI imaging in the diagnosis of Alzheimer's disease

Alzheimer's disease (AD) is the most common form of dementia. Beta amyloid plaques, neurofibrillary tangles, and glucose metabolism reduction are the most prevalent pathological characteristics of AD (Shin et al., 2010). Different imaging modalities have been employed for the diagnosis of AD such as positron emission tomography (PET), computed tomography (CT), and magnetic resonance imaging (MRI). Glucose metabolism reduction and beta amyloid accumulation in the AD patient's brain can be visualized by using PET with 2-[18F]fluoro-2deoxy-D-glucose(FDG) and C-Pittsburgh Compound B (PIB) (Johnson, Fox, Sperling, & Klunk, 2012). However, the spatial resolution of PET systems is relatively low, typically between 5 and 6 mm full-width at half-maximum (FWHM) (Thomas et al., 2011).

Besides glucose metabolism reduction and beta amyloid accumulation, brain atrophy is another biomarker of AD due to neurodegeneration. Structural MRI imaging studies have shown that brain atrophy starts at very early stages of dementia. For example, hippocampal volume can be reduced by 15-30 % at the mild dementia stage of AD (Frisoni, Fox, Jack, Scheltens, & Thompson, 2010). The whole brain volume can be reduced by 6 % by the time a clinical diagnosis is made (Johnson et al., 2012). The degree of atrophy of medial temporal structures such as the hippocampus is suggested to be a diagnostic marker for AD at the mild cognitive impairment stage (Frisoni et al., 2010).

The partial volume effect (PVE) is common in PET/SPECT imaging. It involves a degradation of image quantitative accuracy due to the poor spatial resolution of the imaging system. Structures that have a spatial extent of less than around 2.5 times the FWHM of the imaging system will exhibit reductions in their regional maximum value because of PVEs (Thomas et al., 2011). Therefore, PET imaging of AD patients can be even more severely affected by PVEs due to the reduction of brain volume. In addition, decrease in brain-structure volumes over time will result in increased PVEs over time, thus hampering quantitative comparisons of radiotracer concentration at different stages of AD progression. As a result, it is of great importance to correct for the PVEs in PET imaging of AD patients. In this thesis, we present the effect of different MR protocols on partial volume correction by using an iterative method (Bowsher et al., 2004).

1.2 Partial volume effect in PET/SPECT imaging

PVEs can be defined as the loss of radiotracer activity in small regions due to the poor spatial resolution of the imaging modality. This can be understood as spill-in and spill-out effect (Bettinardi, Castiglioni, De Bernardi, & Gilardi, 2014). Spill-in effect happens when the volume of interest (VOI) has a lower radioactivity concentration than the surrounding tissue, leading to overestimate of the radioactivity concentration inside the VOI. Spill-out effect happens when the VOI has a higher radioactivity concentration than the surrounding tissue, leading to underestimate of radioactivity concentration in the VOI. Either way, the quantitative accuracy of PET/SPECT images suffers from PVEs due to the poor spatial resolution, especially when the diameter of imaging object is close to the FWHM of the imaging system.

1.3 PET image reconstruction methods

1.3.1. Objective Functions

Maximum Likelihood Objective Function

The maximum likelihood objective function has a form of:

$$\Phi(\Lambda; Y) = l(\Lambda; Y)$$

Where, $\Lambda = \{\lambda_j : j = 1, nvox\}$ is the estimated radiotracer distribution, $Y = \{y_i : i = 1, nbin\}$ is the measured projection data, $nvox$ and $nbin$ are the number of image voxels and detector bins, and l is the Poisson log likelihood function.

The probability, P, of the measured projection count, Y, given an estimated radioactivity distribution, Λ, is the product of probabilities for each projection pixel:

$$P\left[\frac{Y}{\Lambda}\right] = \prod_i \frac{\exp\left[-\sum_j a_{ij}\lambda_j\right]\left(\sum_j a_{ij}\lambda_j\right)^{y_i}}{y_i!}$$

Where, α_{ij} is the probability that photon emitted from voxel j will be detected in detector bin i. The Poisson log likelihood function, l, is referred to the natural log of the likelihood function:

$$l(\Lambda; Y) = \sum_i \left(-\sum_j a_{ij}\lambda_j\right) \ln\left[\frac{\left(\sum_j a_{ij}\lambda_j\right)^{y_i}}{y_i!}\right]$$

Penalized Maximum Likelihood Objective Function

The Penalized maximum likelihood objective function has a form of:

$$\Phi(\Lambda; Y) = l(\Lambda; Y) + \beta P$$

Where, $\Lambda, Y\ and\ l$ have the same definition as in the maximum likelihood objective function, P is the penalty function and β is the prior strength for the penalty function. One widely used form for the penalty function involves Gibbs distributions and Markov random fields. In a Markov random field, the probability of a particular voxel value depends only on the voxel values in a neighborhood of that voxel (Zaidi, 2005).

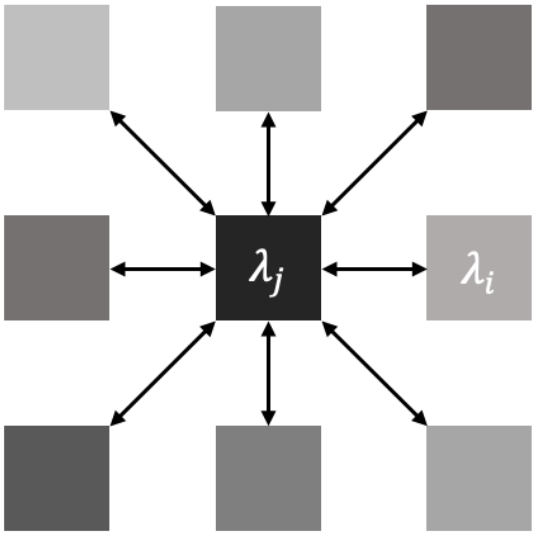

Figure 1 : Illustration of the interaction between the center voxel and it's neighboring voxels.

The interactions are often specified to have a quadratic form:

$$P = -\sum_{i \in N_j} \alpha_{ij} (\lambda_i - \lambda_j)^2$$

Where, $\lambda_i\ and\ \lambda_j$ are the voxel value of voxel i and voxel j, α_{ij} modulates the strength of the interaction between voxel i and voxel j, and N_j contains the neighboring voxels for voxel j.

The simplest way of selecting the neighboring voxels is to select the neighboring voxels isotopically, e.g. as illustrated in Fig.1. This doesn't acquire any additional

anatomical information. However, the problem of this selection is that it may cause strong smoothing over edges when the selected neighboring voxel and the center voxel are in different tissues. This reduces the contrast and increases partial volume effects.

To address this problem, methods have been proposed to incorporate anatomical information such as MRI images into the penalty function. One approach is to turn off or reduce the interactions between voxels in different tissues by setting α_{ij} to zero or to a smaller value. Tissue type can be estimated from an MRI image. A second approach is to select the neighboring voxels which have MRI/CT image intensities closest to that of voxel j (Bowsher et al., 2004).

1.3.2. ML-EM

Maximum likelihood-expectation maximization (ML-EM) is an iterative method of PET and SPECT image reconstruction (Lange & Carson, 1984.; Shepp & Vardi, 1982). The EM algorithm involves two steps: First, an initial image is estimated after the projection data is collected. The initial estimated image does not need to be very accurate, it can just be set to a constant positive value, like all ones, throughout the entire image. Next, MLEM forward projects the estimated image to calculate an estimate of the projection data. Then, it compares these estimated projection data with the measured projection data to get an updated estimate of the contribution, to the image, from each projection bin. The contributions are then applied to generate an updated estimate of the image. The algorithm repeats itself for a user-specified number of iterations.

1.3.3. OSEM

Ordered subsets expectation maximization (OSEM) is an accelerated form of ML-EM algorithm (Hudson & Larkin, 1994). The advantage of OSEM is that it reduces the computation time by dividing the projection data into subsets. For example, assume we have the projection data of the object in 4 different angles. We divide the projection data into 2 subsets, each subset contains the projection data of 2 projection angles. Then, ML-EM is applied to the projection data in subset 1 to obtain an estimate image. Next, the estimate image is entered as the basis for ML-EM applied to the projection data in subset 2. Thus, the computation time is reduced in proportion to the number of subsets.

OSEM and ML-EM are algorithms for optimizing the maximum likelihood objective function. Low and middle frequency components are obtained at low iterations (Alessio, A et al., 2007). As the number of iterations increases the high frequency components are reconstructed but the noise level in the image also increases (Ahn et al., 2015). Therefore, usually the algorithm is stopped before the ML estimate is achieved. In some cases, post-filtering is applied to reduce the noise in the reconstructed image.

1.3.4. MAP/ICD

Maximum *a-posterior*/iterative coordinate decent (MAP/ICD) is an alternative algorithm to ML-EM and OSEM. MAP/ICD employs a penalty function to control the quality of reconstructed PET images (Ahn et al., 2015). It is also known as penalized likelihood (PL) image reconstruction. The ICD algorithm is used in this project to optimize the penalized maximum likelihood objective function mentioned in section 1.3.1.

1.3.5. Research Gap and Project Aims

Many methods have been proposed to incorporate anatomical information (MRI/CT) into the reconstruction of PET/SPECT images in order to correct the partial volume effects (Atre, Vunckx, Baete, Reilhac, & Nuyts, 2009). However, generally only one single MRI sequence (T1 or T2 weighted MRI) has been investigated. In this project, 6 different MRI protocols are compared to investigate the effect of MRI sequence on PVC for PET/SPECT imaging.

2. Methods

2.1. Software

The software used for PET and MR simulation was SPECT-MAP (Bowsher, DeLong, Turkington, & Jaszczak, 2006) and MRiLab (Liu, Velikina, Block, Kijowski, & Samsonov, 2017) respectively. SPECT-MAP was used to simulate PET/SPECT projection data and to reconstruct PET/SPECT images from that projection data. Image reconstruction, using SPECT-MAP, was performed by two algorithms: ordered subsets expectation maximization (OSEM) and maximum *a-posterior*/iterative coordinate decent (MAP/ICD) algorithm. MRiLab is a numerical MRI simulator with a Matlab interface. It allows the user to modify the scan parameters to simulate different MRI scans. Here, MRiLab was used to simulate T1-, T2-, proton-density- (PD-) weighted and inversion recovery MR brain images.

2.2. Brain Phantom

MRiLab provides a realistic, high resolution, digital, volumetric segmentation model of the human brain. This segmentation has a matrix size of 216x180x180, with an isotropic voxel width of 1mm. The segmentation was utilized to generate MRI images via MRiLab and to generate a radiotracer phantom, thus providing perfect registration of MRI and PET images. MRiLab also provides MRI tissue properties of up to 8 different tissues: cerebral spinal fluid (CSF), white matter (WM), gray matter (GM), fat, muscle, skin, skull, and connective tissue. Table 1 gives the MRiLab tissue properties of CSF,

WM and GM that were used for this study. Figure 2 shows an example of the digital brain phantom. The white structure in between CSF and WM is the connective tissue.

Table 1 Tissue properties

Tissue type	Proton Density Rho	T1(s)	T2(s)	T2*(s)
GM	0.8	0.95	0.1	0.05
WM	0.65	0.6	0.08	0.04
CSF	1	4.5	2.2	1.1

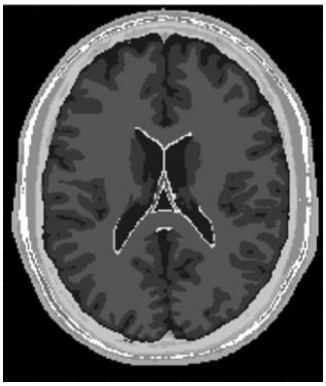

Figure 2: High resolution 3-D digital segmentation model of the brain provided by MRiLab.

2.3. MRI Images

The digital segmentation has 180 slices, and the MRI images were simulated from slices 85-90. The MRI images were 216mmx180mm with 3 slices, each slice being 2mm thick. Each MRI slice corresponded to 2 slices of the digital segmentation. MRI voxel widths in the phase- and frequency-encoding directions were both 1 mm, while MRI voxel width in the axial direction was 2mm. All the MR images were simulated assuming a 1.5T magnetic field. Spin-echo was chosen to generate T1-, T2-, and proton-

density- (PD-) weighted MRI images. For inversion recovery images, the inversion time TI was chosen according to:

Equation 1

$$TI = \ln(2) \times T_1,$$

where, T_1 is the longitudinal relaxation time for the tissue whose signal is suppressed: GM, WM, or CSF (P. 433, Prince & Links, 2015).

The longitudinal magnetization and transverse magnetization decay of GM, WM and CSF are described by:

Equation 2

$$M_z(t) = M_0 \times \left(1 - e^{-\frac{t}{T_1}}\right) + M_z(0^+)e^{-\frac{t}{T_1}}$$

and

Equation 3

$$M_{xy}(t) = M_{xy}(0^+) \times e^{-\frac{t}{T_2}}$$

(P. 424, Prince & Links, 2015)

Where, $M_z(0^+)$ is the longitudinal magnetization immediately after the α pulse, and $M_{xy}(0^+)$ is the transverse magnetization immediately after the α pulse. $M_z(0^+)$ is given by:

Equation 4

$$M_z(0^+) = M_z(0^-)\cos(\alpha),$$

where α is the flip angle, and $M_z(0^-)$ is the longitudinal magnetization before each pulse.

The transverse magnetization immediately after the α pulse is given by:

Equation 5

$$M_{xy}(0^+) = M_z(0^-)\sin(\alpha)$$

The equilibrium magnetization M_0 is given by:

Equation 6

$$M_0 = \frac{B_0\gamma^2h^2}{4kT} \times P_D,$$

where B_0 is the external static magnetic field, k is Boltzmann's constant, h is Planck's constant, T is temperature, and P_D is proton density. Different tissues have different proton densities and thus have different magnetizations at equilibrium. Since B_0, k, h, and T are constant, we used P_D to represent M_0 for each tissue type.

The steady-state value of longitudinal magnetization before each pulse is given by:

Equation 7

$$M_z(0^-) = M_0 \frac{1-e^{-\frac{TR}{T_1}}}{1-\cos(\alpha)e^{-\frac{TR}{T_1}}}.$$

(P. 474, Prince & Links, 2015)

The transverse magnetization at echo time TE which is the source of NMR signal for a steady-state pulse sequence can be written as:

Equation 8

$$M_{xy} = M_0\sin(\alpha) \times e^{-\frac{TE}{T_2}} \frac{1-e^{-\frac{TR}{T_1}}}{1-\cos(\alpha)\,e^{-\frac{TR}{T_1}}}$$

(P. 474, Prince & Links, 2015)

where, M_0 is given by Equation 6.

T1 recovery and T2 decay curves of each tissue were plotted in order to select TR and TE for good contrast in each case. For T1-, T2-, and PD- weighted MRI images, the T1 recovery and T2 decay curves are plotted as a function of time, based on equations 7 and 8.

For inversion recovery images, we utilized the MRiLab default repetition time, which $T_R = 15000ms$. This repetition time is much longer than the T1 values for GM, WM, and CSF. Therefore, the longitudinal magnetization of each tissue is assumed to reach the equilibrium magnetization (Equation 6) prior to the π-pulse. The T1 recovery and T2 decay curves for inversion recovery images are plotted based on equations 2 and 3, which are:

Equation 9

$$M_z(t) = M_0 \times \left(1 - e^{-\frac{t}{T_1}}\right) + M_0 e^{-\frac{t}{T_1}},$$

and

Equation 10

$$M_{xy}(t) = M_z(TI) \times e^{-\frac{t}{T_2}}$$

Six sets of MRI images were generated using MRiLab: T1-, T2-, PD-, and 3 inversion recovery images. For T1-, T2 and PD-weighted images, TR and TE values were chosen based on the T1 recovery and T2 decay plots for each simulation to maximize contrast between GM, WM and CSF.

2.4. PET Phantom

The same slices of the brain phantom were chosen to build the radiotracer phantom. For this study, only the uptake of radiotracer in the CSF, WM, and GM are considered and the distribution of radiotracer in each tissue type is assumed to be uniform. For many radiopharmaceuticals, the baseline of gray matter radiopharmaceutical concentration is about 4 times the baseline white matter concentration, while CSF usually has zero radiotracer concentration (Lipinski, Herzog, Rota Kops, Oberschelp, & Muller-Gartner, 1997). Therefore, 0 $\mu Ci/ml$, 1$\mu Ci/ml$, 4 $\mu Ci/ml$ of radiotracer concentration were assigned to CSF, WM, and GM respectively. Two versions of the radiotracer phantom were generated, one on a fine grid of voxels that were 1-mm-wide squares transaxially and 2 mm thick axially, and one on a course grid of voxels that were 2-mm-wide squares transaxially and 2 mm thick axially. The radiotracer phantom is shown in Figure 3. It is constructed from the aforementioned 6 slices of the brain segmentation, with each fine-grid radiotracer-phantom slice constructed from 2 slices of the brain segmentation. Hence some voxels in the fine-grid have a half-and-half mixture of two tissue types. The fine-grid radiotracer phantom thus has a matrix size of 216x180x3, and the fine-grid phantom voxels are 1-mm-wide transaxially and 2 mm thick axially.

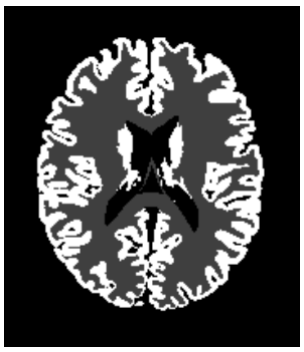

Figure 3: One slice of the radiotracer phantom. The radiotracer concentration in CSF, WM, and GM are 0 $\mu Ci/ml$, 1 $\mu Ci/ml$, 4 $\mu Ci/ml$.

A course-grid radiotracer phantom was generated from the fine-grid radiotracer phantom for purposes of comparing the phantom with reconstructed PET/SPECT images. The course grid has 108x90x3 voxels, with an isotropic voxel width of 2mm. The value in each course-grid phantom voxel is the average of values in 4 fine-grid phantom voxels. Therefore, the course-grid phantom has many different voxel values.

Since the same brain segmentation was used to generate the MR images and PET phantom, the registration between MR and PET images is perfect.

2.5. PET Projection Data Simulation and Image Reconstruction

2.5.1. Forward Projection and Acquisition Modeling

PET/SPECT projection data were computer-simulated with SPECT-MAP using the fine-grid radiotracer phantom. Data were acquired into 2mm by 2mm-wide detector bins at 120 projection angles equally spaced over 360°. The noisy data were obtained by sampling from a Poisson distribution at each bin. The expected value of the Poisson distribution was determined by scaling the total counts from 1.2×10^3 to 5×10^5. Detector spatial resolution was modeled as 6mm full-width-at-half-maximum using the

methods described in (Bowsher et al., 2006). Attenuation and scatter effects were not simulated.

2.5.2. PET Image Reconstruction

The PET/SPECT images were reconstructed from the noisy projection data on the course grid. All reconstructions were thus into three slices of 2mm by 2mm by 2mm voxels. As a result, each PET/SPECT slice had a size of 108x90, and each slice was 2 mm thick.

2.5.3. OSEM reconstruction

Since Ordered-Subsets Expectation Maximization (OSEM) is the most widely used method for reconstruction of clinical PET/SPECT images, PET/SPECT images were reconstructed by the OSEM algorithm using 10 subsets and up to 16 iterations. The disadvantage of OSEM is that the reconstructed image is blurry at low iterations and noisy at high iterations.

2.5.4. MAP/ICD reconstruction with Isotropic Prior

PET/SPECT images were also reconstructed using the MAP/ICD algorithm (Ahn et al., 2015) with an isotropic prior. The 4^{th} iteration of OSEM image reconstruction was selected as the initial estimate image. Isotropic prior means the neighboring voxels selected for smoothing were chosen isotopically around the target voxel. The weights α_{ij} were the same for all i and j. A quadratic penalty function was used. Twenty neighboring voxels were selected.

2.5.5. MAP/ICD reconstruction with MRI Based Prior

For PET image reconstructed using the MAP/ICD algorithm with MRI-based prior, the 4th iteration of OSEM image reconstruction was selected as the initial image estimate for the MAP/ICD algorithm. Neighboring voxels selected for smoothing were chosen based on their MRI signal intensity, such that the selected voxels tended to have similar MRI signal intensity as the target voxel (Bowsher et al., 2004). The weights α_{ij} were the same for all selected smoothing interactions, and the smoothing interactions were quadratic.

3. Results

3.1. MRI images

3.1.1. T1-Weighted MR image

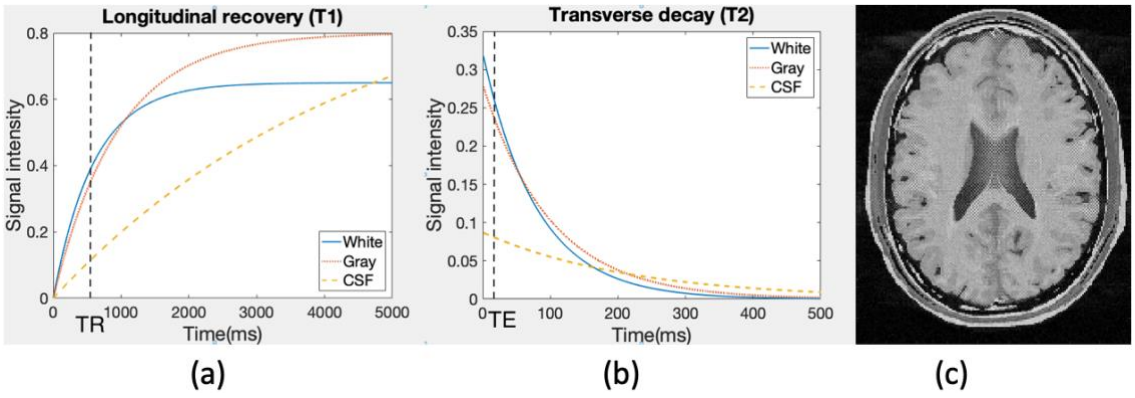

Figure 4: (a) Longitudinal magnetization $M_Z(0^-)$ plotted versus TR and (b) transverse decay as a function of time and (c) the simulated T1-weighted MR image.

A short TR and a short TE were selected to maximize the T1 contrast and minimize the T2 contrast between the three different tissue types in the T1-weighted image. The T1-weighted MR image shown was obtained using TR = 410 ms, TE = 10 ms, and flip angle $\alpha = \pi/2$. TR value was selected to maximize the T1 contrast between GM and WM according to plot (a). The selected TR is close to the T1 value of WM and GM but is much less than the T1 value of CSF. Therefore, the longitudinal magnetization recovered in CSF was much less than in WM and GM. As a result, the CSF signal was much smaller than the WM and GM signal. As shown in Figure 4, the WM and GM are bright while the CSF is dark.

The transverse magnetizations M_{xy} of each tissue at time TE were as follows:

Mxy_CSF(t = TE) = 0.0832

Mxy_GM(t = TE) = 0.2537

Mxy_WM(t = TE) = 0.2840

3.1.2. T2-Weighted MR image

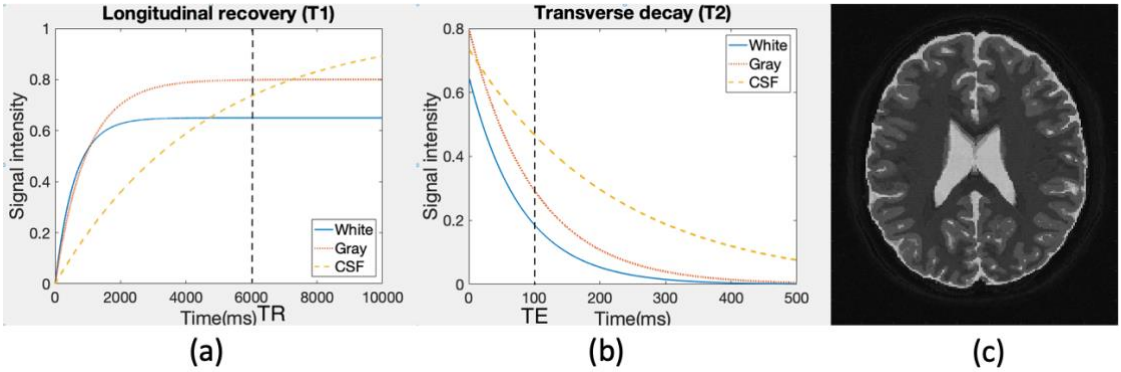

Figure 5: (a) Longitudinal magnetization $M_Z(0^-)$ plotted versus TR, (b) transverse decay as a function of time, and (c) the simulated T2-weighted MR image.

For the T2-weighted image, relativy long TR and TE values were selected to minimize the T1 contrast and maximize the T2 contrast between the three different tissue types.The T2-weighted MR image shown was obtained using TR = 6000 ms, TE = 100 ms, and $\alpha = \pi/2$. TR value was selected to minimize the T1 contrast between CSF, GM, and WM. TE value was selected to maximize the T2 contrast between CSF, GM, and WM. The use of larger TR here increases the maximum signal strength.

The transverse magnetization M_{xy} of each tissue at time TE were as follows:

Mxy_CSF(t = TE) = 0.4674

Mxy_GM(t = TE) = 0.2938

Mxy_WM(t = TE) = 0.1862

3.1.3. Proton-Density Weighted MR image

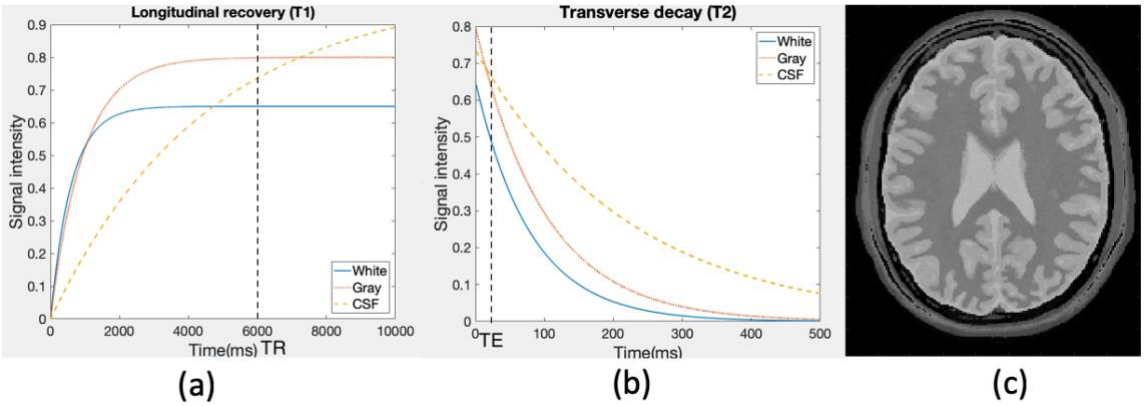

Figure 6: (a) Longitudinal magnetization $M_Z(0^-)$ plotted versus TR, (b) transverse decay as a function of time, and (c) the simulated PD-weighted MR image.

Proton-Density Weighted images minimize the T1 and T2 contrast. Signal strength is influenced largely by proton-density. The PD-weighted MR image is the result of using TR = 6000 ms, TE = 20 ms, and $\alpha = \pi/2$. TR value was selected to minimize the T1 contrast between CSF, GM, and WM. TE value was selected to minimize the T2 contrast between CSF, GM, and WM. Here the relative proton density values of CSF, WM, and GM are 1, 0.65, and 0.8 respectively.

The transverse magnetization M_{xy} of each tissue at time TE were as follows:

Mxy_CSF(t = TE) = 0.6724

Mxy_GM(t = TE) = 0.6538

Mxy_WM(t = TE) = 0.5062

3.1.4. Inversion Recovery MR image

ZeroCSF image

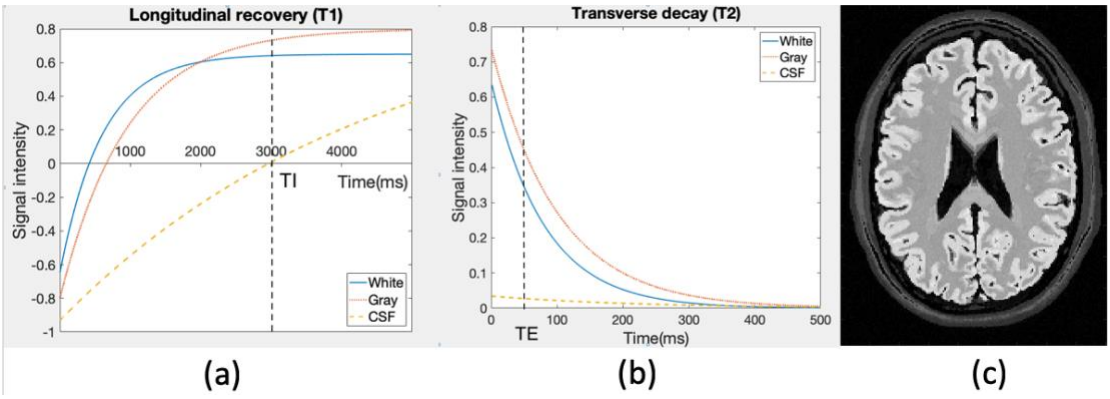

Figure 7: (a) Longitudinal recovery and (b) transverse decay as a function of time. (c) The simulated ZeroCSF MR image.

An inversion recovery pulse was used to generate an inversion recovery image which suppresses the signal from either CSF, GM or WM. After a 180 RF pulse was applied, the longitudinal magnetization was inverted, that is

Equation 11

$$M_z(0^+) = -M_0 \,,$$

where the magnetization prior to the 180 RF pulse is assumed to be the equilibrium magnetization M_0. This assumption is based on the long, 15,000 ms T_R value utilized to simulate the inversion recovery images. The longitudinal magnetization recovers in exponential form as described by Equation 2. Substituting Equation 11 into Equation 2 yields:

Equation 12

$$M_z(t) = M_0 \times (1 - 2e^{-\frac{t}{T_1}})$$

Let $M_z(t) = 0$ and solve the equation. we have $t = \ln(2) \times T_1$ which is the inversion time. The ZeroCSF MR image shown was obtained using TR = 15000ms, the inversion time TI = 3119ms, and TE = 50ms. Since the signal of CSF was suppressed, the contrasts between WM and CSF and between GM and CSF were large in the ZeroCSF inversion recovery image.

The transverse magnetizations M_{xy} of each tissue at time TE were as follows:

Mxy_CSF(t = TE) = 0.0274

Mxy_GM(t = TE) = 0.4488

Mxy_WM(t = TE) = 0.3441

Similarly, we also simulated the ZeroGM and ZeroWM MRI images.

ZeroGM image

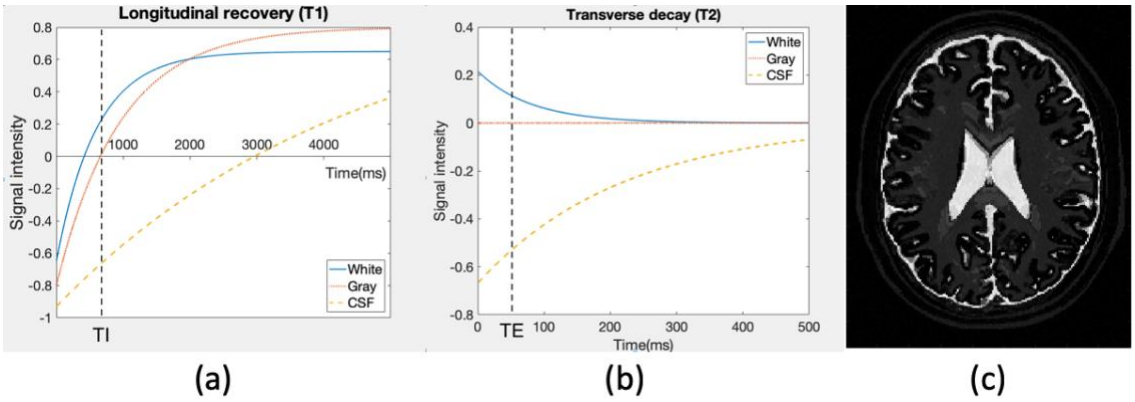

Figure 8: The plot of (a) longitudinal recovery and (b) transverse decay as a function of time and (c) the resulting ZeroGM MR image.

The ZeroGM MR image shown was obtained using TR = 15000ms, TE = 50ms, and inversion time TI = 658ms.

ZeroWM image

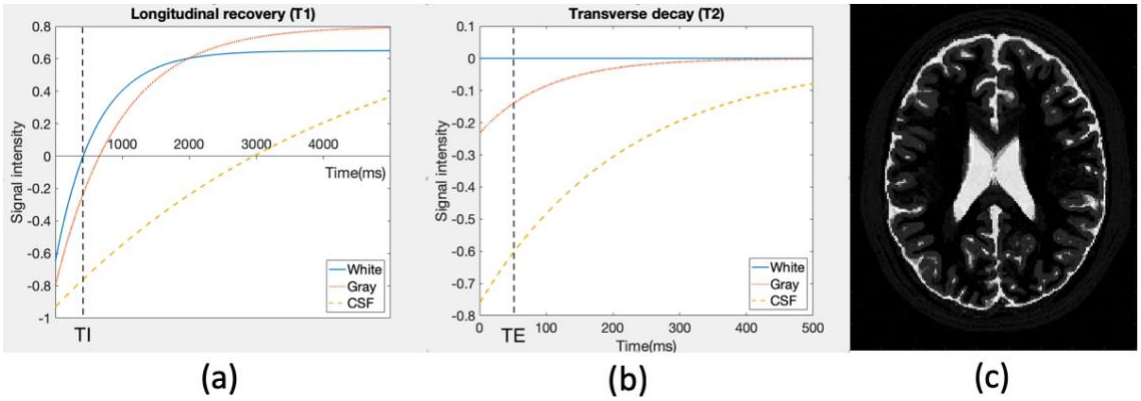

Figure 9: The plot of (a) longitudinal recovery and (b) transverse decay as a function of time and (c) the resulting ZeroWM MR image.

The ZeroWM MR image shown was obtained using TR = 15000ms, TE = 50ms, and inversion time TI = 416ms.

3.2. Contrast

3.2.1. Theoretical contrast

Transverse magnetization at TE

The contrast between GM, WM, and CSF were computed based on the T2-decay plots. We obtained the transverse magnetization M_{xy} at time TE for each tissue and calculated the theoretical contrast between each tissue based on equation:

Equation 13

$$Contrast = \frac{(M_{xy}A - M_{xy}B)}{(M_{xy}A + M_{xy}B)/2}$$

Table 2 Transverse magnetization at time TE

Protocol	T1	T2	PD	ZeroCSF	ZeroGM	ZeroWM
M_{xy}(GM) at TE	0.2537	0.2938	0.6538	0.4488	-2.4×10^{-4}	-0.1411
M_{xy}(WM) at TE	0.2840	0.1862	0.5062	0.3441	0.1155	6.47×10^{-5}
M_{xy}(CSF) at TE	0.0832	0.4674	0.6724	0.0274	-0.5325	-0.6060

Table 3 Theoretical contrast between each tissue

Protocol	T1	T2	PD	ZeroCSF	ZeroGM	ZeroWM
C_WM_CSF	1.0935	-0.8604	-0.2820	1.7048	-3.1081	-2.0004
C_GM_CSF	1.0121	-0.4563	-0.0281	1.7697	-1.9981	-1.2445
C_GM_WM	-0.1125	0.4481	0.2545	0.2642	-2.0087	2.0018

3.2.2. Contrast in MRI image

Three segmentation maps were created from the 3D segmentation model of Brain for CSF, GM, and WM. Those segmentation maps were used to calculate the mean value of each three tissue in the actual MRI images. The contrasts were then calculated using the mean value of each tissue by equation 13. Table 4 give the actual contrast in MRI images. Although the values were not exactly same for the theoretical contrast and

actual contrast in the image, the did follow the same pattern. The difference between the theoretical contrast and actual contrast could be caused by the noise in the MRI images.

Table 4 Actual contrast in MRI images

Protocol	T1	T2	PD	ZeroCSF	ZeroGM	ZeroWM
C_WM_CSF	0.7849	-1.0717	-0.2502	1.4670	-1.3228	-1.8388
C_GM_CSF	0.6125	-0.7228	-0.0601	1.5331	-1.6553	-1.2540
C_GM_WM	-0.1960	0.4327	0.1908	0.1510	-0.7346	1.3808

3.3. Comparison between OSEM and MAP/ICD with isotropic Prior

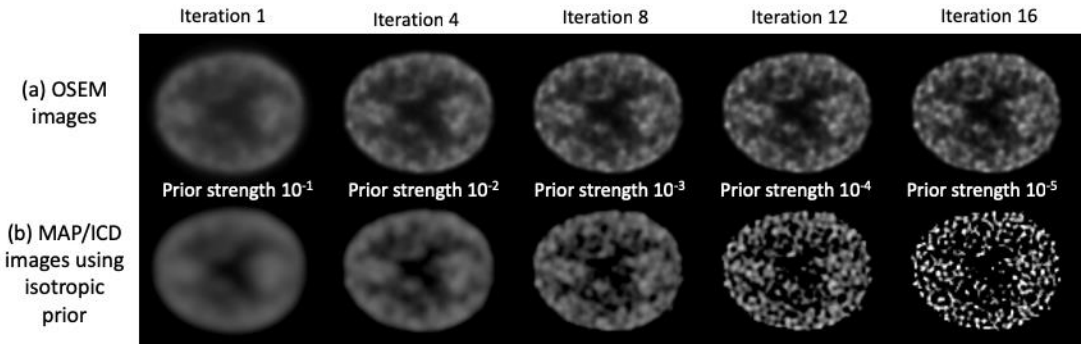

Figure 10: (a) OSEM images at different number of iterations. (b) MAP/ICD images varying with prior strength.

In Fig. 10, PET images reconstructed by the MAP/ICD algorithm with an isotropic prior are compared to the PET images reconstructed by the OSEM algorithm. The MAP/ICD images are shown at convergence (i.e. at a number of iterations sufficient for convergence) and with varying prior strength. The OSEM images are shown at various number of iterations. The figure suggests that MAP/ICD and OSEM images may be similar once the prior strength range is matched with OSEM iterations. For example,

the OSEM image at iteration 4 and MAP/ICD image at prior strength of 10^{-2} are similar. The overall conclusion is that OSEM and MAP/ICD images with isotropic prior are blurry and/or noisy with blur more severe at lower OSEM iterations and lower MAP/ICD prior strengths.

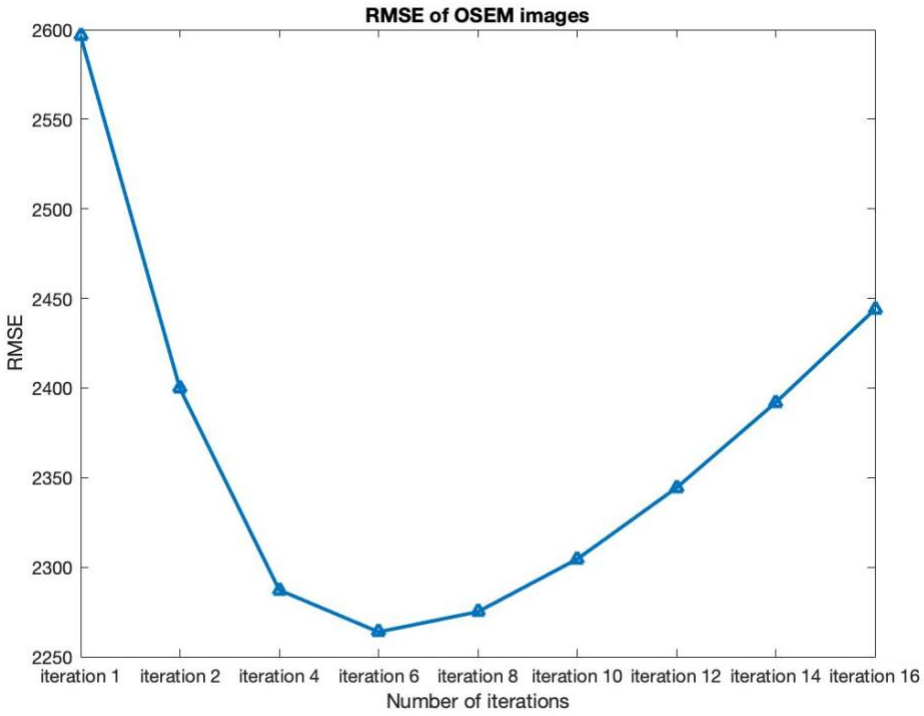

Figure 11: RMSE values of OSEM images versus number of iterations.

Figure 11 shows that RMSE first decreases as the number of iterations increases, reaches the lowest RMSE at iteration 6, and then increases as the number of iterations continues to increase. For the OSEM image, low and middle frequency components are reconstructed at lower iterations (Alessio, A et al., 2007). As the number of iteration increases, the noise level of the PET image also increases which results in the increase of RMSE value at higher iterations (Ahn et al., 2015). Therefore, in practice, OSEM is stopped early before the image gets too noisy.

3.4. Comparison between the PET-T1, PET-T2, PET-PD, and PET-Inversion Recovery Images

Figure 12 shows the PET images reconstructed with different MRI images using the method (Bowsher et al., 2004), with 20 voxels out of 100 neighboring voxels utilized for smoothing.

Compared with the OSEM and MAP/ICD images obtained by using an isotropic prior in Figure-10, the PET images reconstructed using anatomical information in Figure-12 show better contrast and less noise. Visually, the PET images reconstructed with the ZeroCSF prior gave the PET image that visually appears to match best with the PET phantom. It has a good contrast between WM and GM, and the CSF pockets in GM are clearly apparent and have good contrast with surrounding GM tissue. PET images reconstructed with T2, PD and ZeroWM MRI images are similar to one another in image quality, but relative to the PET phantom and the ZeroCSF PET image, these images have poor contrast between CSF pockets and surrounding GM tissue, and they have less contrast between GM and WM. PET images reconstructed with the T1 image had a better GM and CSF contrast, and some of the CSF pockets in GM were reconstructed, but the WM region was very noisy. PET images reconstructed with the ZeroGM image had noticeably worse performance in the GM region. The ZeroGM PET image shows a washout in the peripheral region while the ZeroCSF PET image doesn't.

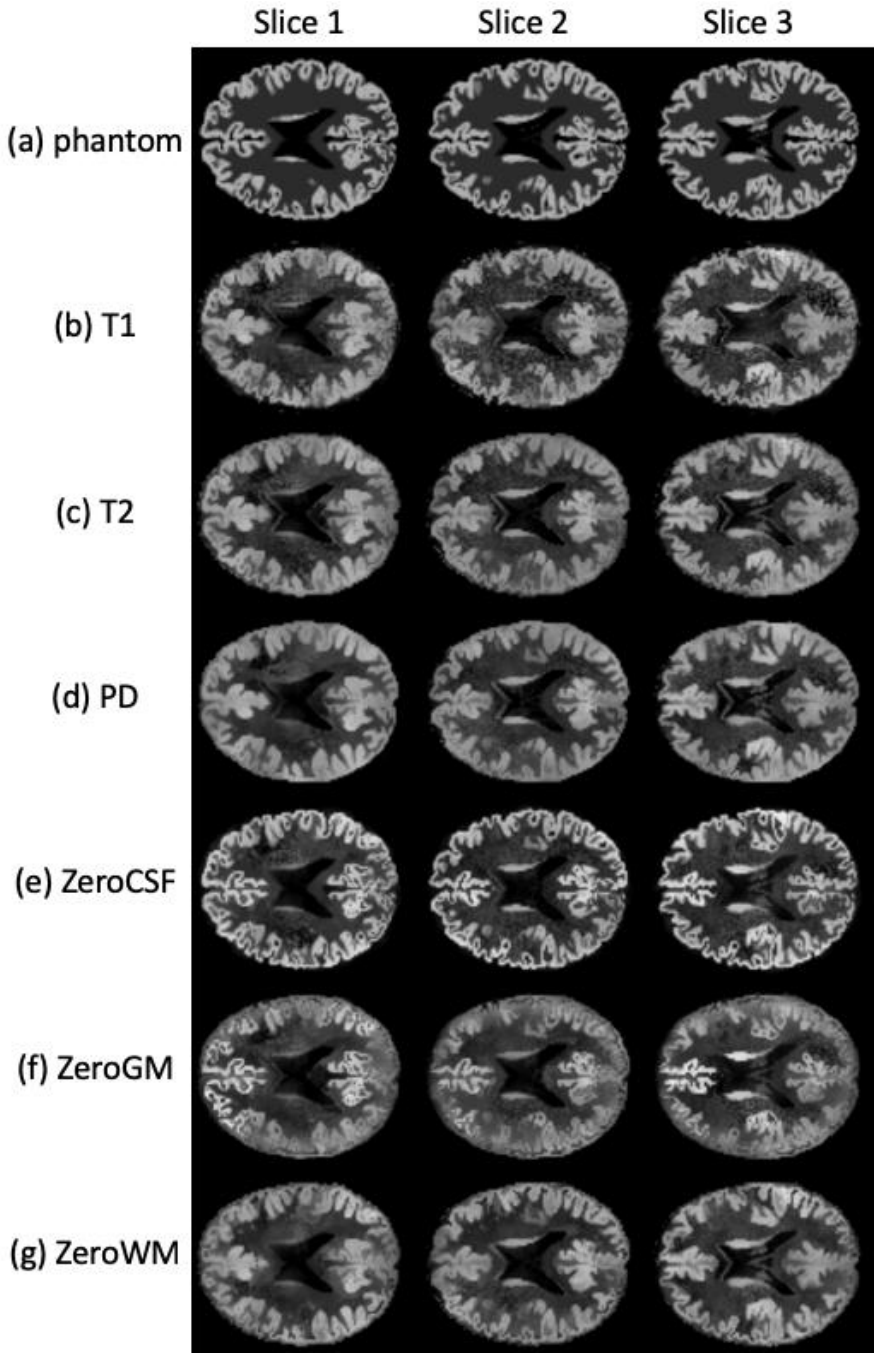

Figure 12: (a) PET phantom and (b-g) PET image reconstructed with (b) T1, (c) T2, (d) PD, (e) ZeroCSF, (f) ZeroGM and (g) ZeroWM MR prior images.

3.5. RMSE calculation

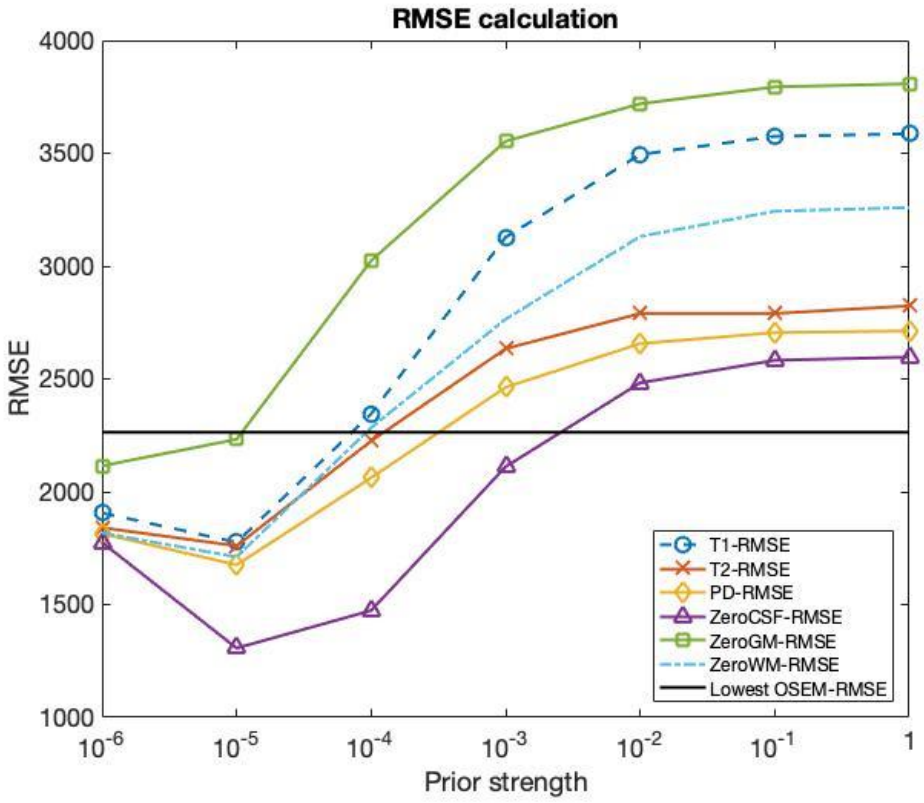

Figure 13: RMSE of PET images versus prior strength.

The Root Mean Square Error was calculated for each type of PET image as a function of prior strength by

Equation 14

$$RMSE = \sqrt{\frac{\sum_{j=1}^{nvox}(\lambda_j - t_j)^2}{nvox}},$$

where, $\Lambda = \{\lambda_j : j = 1, nvox\}$ is the estimated PET image, $nvox$ is the number of image voxels, $T = \{ t_j : j = 1, nvox\}$ is the true PET image, which is the course-grid PET phantom in this study.

The lowest RMSE value for OSEM images is shown as the horizontal line. The plot shows that for each type of PET image except ZeroGM, the lowest minimal RMSE value is achieved at a prior strength of $1x10^{-5}$. Among all the PET images, the ZeroCSF prior gives the smallest RMSE values at all prior strengths. This is consistent with the qualitative observation that in Figure-12, the ZeroCSF image appears to match best with the PET phantom. Another point worth noticing was that T1 and ZeroGM gave noticeably worse RMSE at higher prior strength.

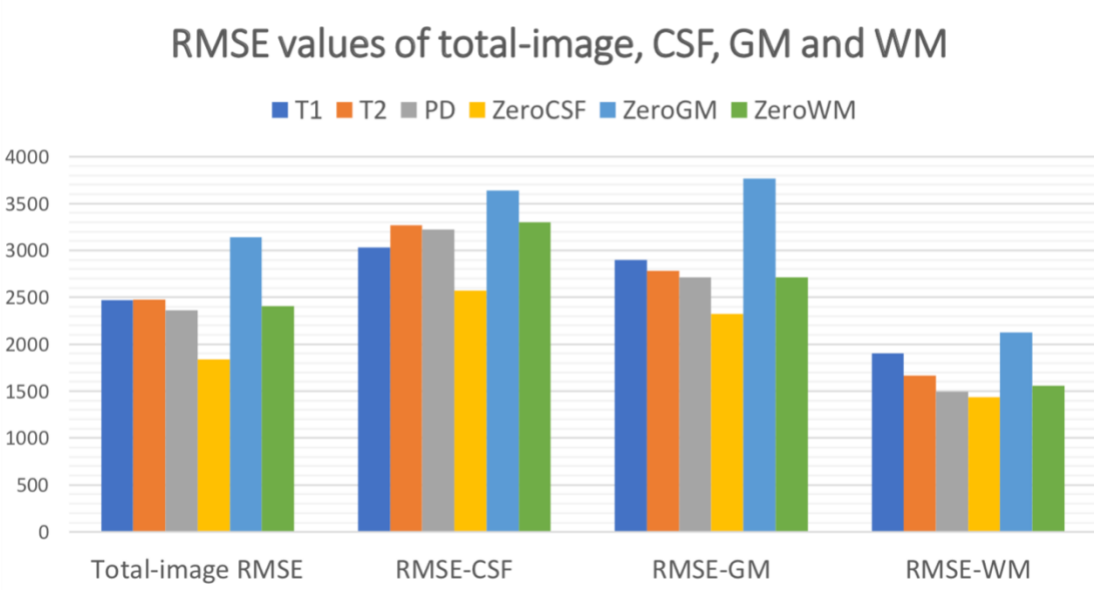

Figure 14: RMSE values of total-image, CSF, GM, and WM for each protocol when selecting 20 out of 100 voxels for smoothing.

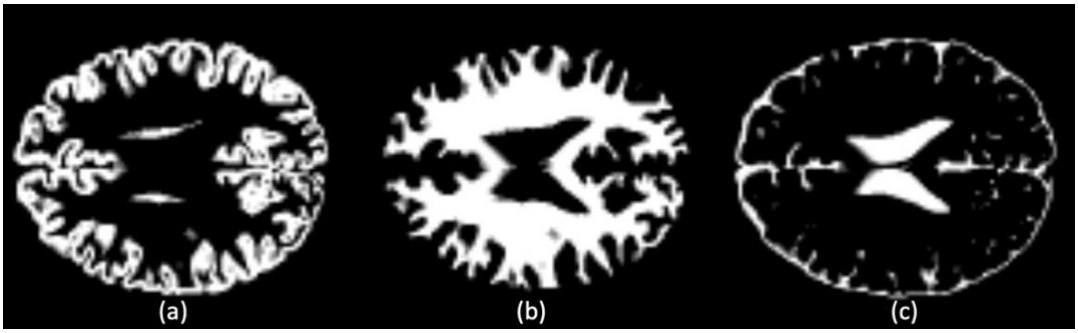

Figure 15: Segmentation maps of (a) GM, (b) WM and (c) CSF used for RMSE calculation.

The RMSE values of CSF, GM, and WM were calculated separately for each protocol at the overall optimal prior strength 10^{-5}. The PET/ZeroCSF image had the lowest RMSE values for all tissue types. Compared with T2 and PD, the T1 prior gave a lower RMSE for CSF but had a worse RMSE for WM region, which is consistent with the visual appearance of the PET images in Figure 12.

Figure 15 shows the segmentation maps used to calculate the RMSE values for each region. The voxel value in segmentation maps is ranging from 0 to 1, which represents the fraction of each tissue type in that voxel. For example, the equation to calculate the RMSE value for CSF is:

$$RMSE - CSF = \sqrt{\frac{\sum_{j=1}^{nvox_{CSF}} [\gamma_j (\lambda_j - t_j)^2}{nvox_{CSF}}},$$

Where, $\Gamma = \{\gamma_j : j = 1, nvox_{CSF}\}$ is the segmentation map for CSF, $nvox_{CSF}$ is the number of CSF voxels, which have non-zero voxel values in the CSF segmentation map, and γ_j is the faction of CSF in voxel j.

3.6 The effect of selecting different numbers of neighboring voxels on PET image reconstruction

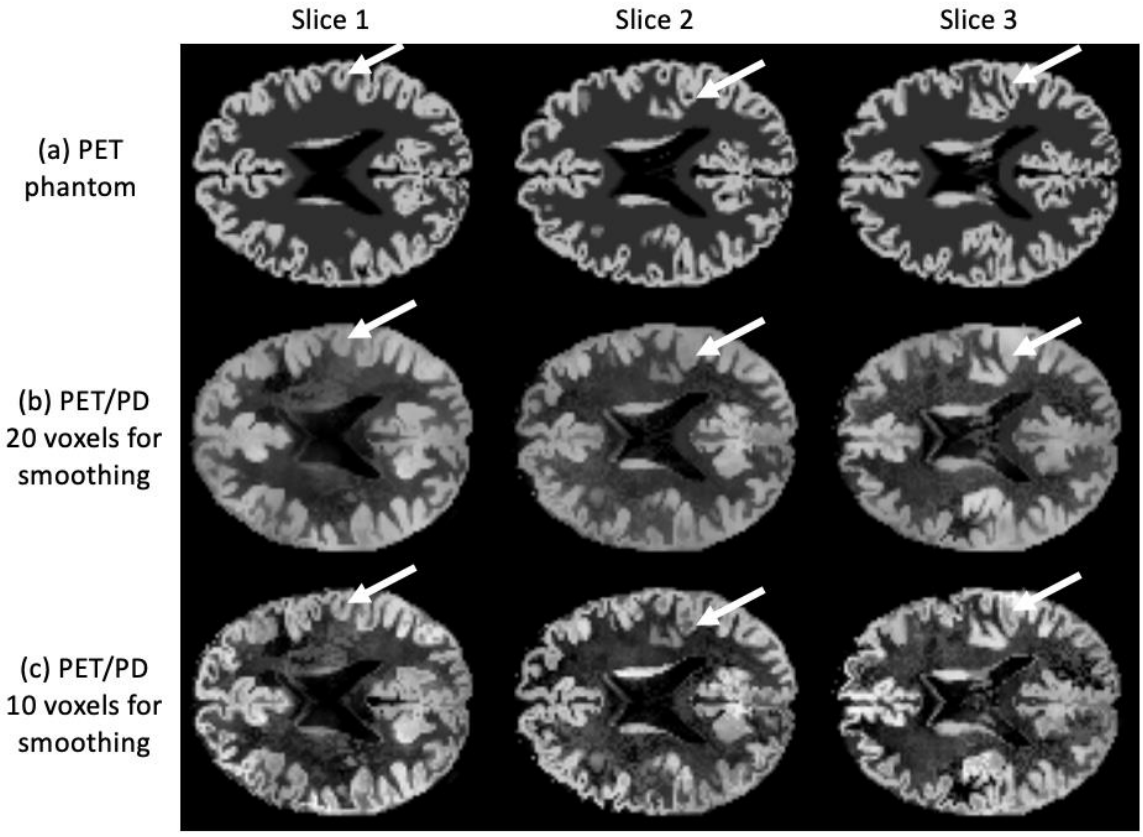

Figure 16: (a) The PET phantom. (b) PET images, 20 out of 100 voxels selected for smoothing. (c) PET images, 10 out of 100 voxels selected for smoothing.

When 20 out of 100 neighboring voxels were selected for smoothing, PET/PD images had poor contrast between CSF pockets and surrounding GM tissue. As pointed out by the arrows in the figure above, the CSF pockets surrounded by GM tissue seen in PET phantom are not visible in the PET/PD image. This might be due to insufficient (i.e. less than 20) CSF voxels in and around the CSF pockets leading to the use of GM voxels for CSF smoothing. When the number of voxels for smoothing is reduced from 20 to 10, the CSF pockets in GM are visible in the PET/PD image as shown in Figure-16-(c) and the contrast between CSF pockets and surrounding GM tissue is also increased. Figure

17 compares the phantom with PET images reconstructed using 10 out of 100 neighbors for T1-, T2-, and PD-weighted MRI images. The contrast of CSF pockets and surrounding GM is generally improved as compared to the 20/100 results shown in figure 12. However, PET/ZeroCSF and PET/ZeroGM images were not sensitive to the selection of numbers of voxels for smoothing as shown in Figure 18. This may be because the contrast between CSF pockets and surrounding GM is already very good when 20 out of 100 neighboring voxels were selected of CSF smoothing. Therefore, reducing the number of selected neighboring voxels doesn't improve the CSF-GM contrast very much.

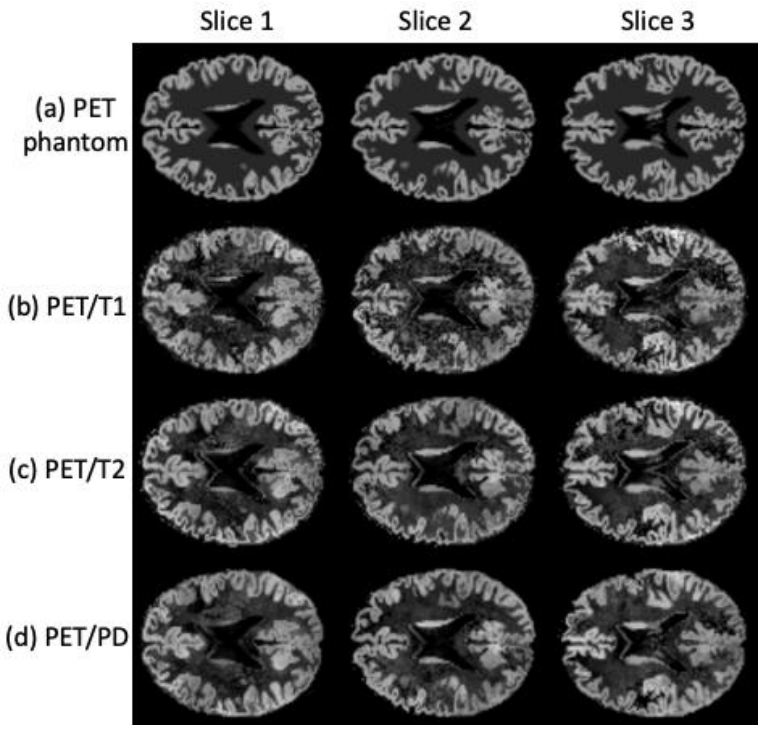

Figure 17: (a) PET phantom and (b-d) PET images reconstructed with (b) T1, (b) T2 and (d) PD MRI image, 10 out of 100 voxels selected for smoothing.

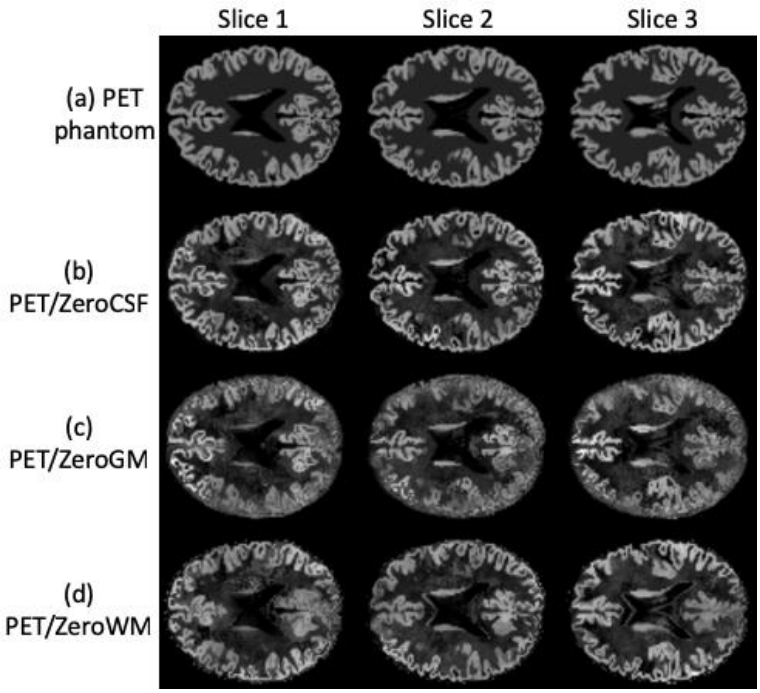

Figure 18: (a) PET phantom and (b-d) PET images reconstructed with (b) ZeroCSF, (c) ZeroGM and (d) ZeroWM, 10 out of 100 voxels selected for smoothing.

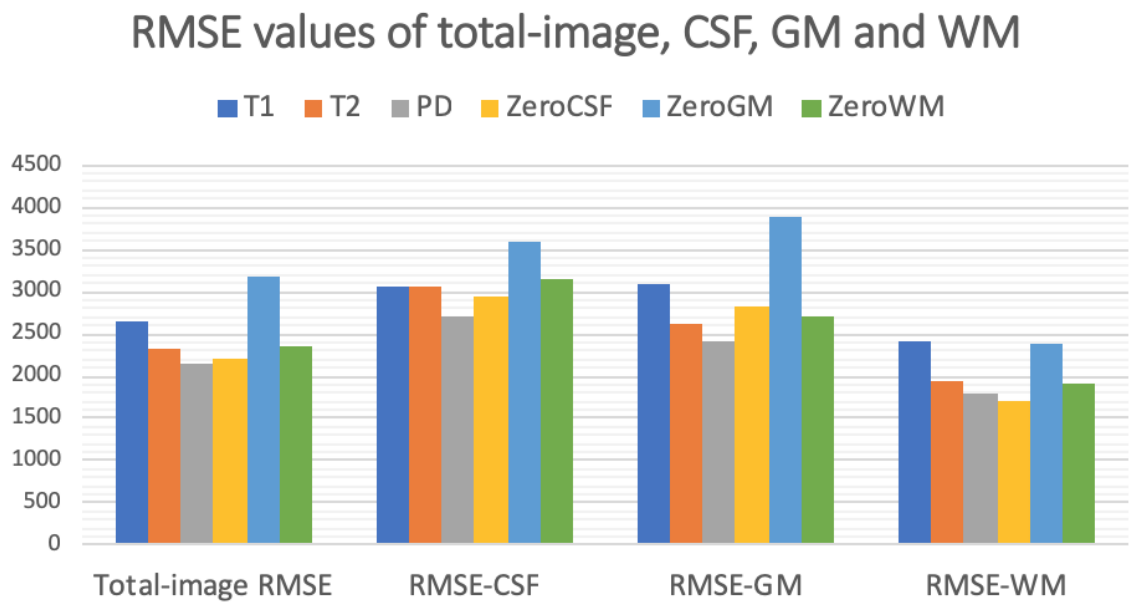

Figure 19: RMSE values of CSF, GM, and WM for each protocol when selecting 10 out of 100 neighboring voxels for smoothing.

The RMSE values of CSF, GM, and WM were calculated again after reducing the number of neighboring voxels selected for smoothing from 20 to 10. In this case, the ZeroCSF prior still gives the lowest RMSE for WM, but the PD prior gives the lowest RMSE for both CSF and GM. This is consistent with visual appearance of the PET image in Figure 16. Many of the CSF pockets are visible when selecting 10 voxels for smoothing which are not visible in the case of selecting 20 voxels for smoothing.

3.7 The effect of the noise level in MRI image on PET image reconstruction

Another possibility of the poor contrast between the CSF pockets and surrounding GM tissue in PET/PD images could be that the PD MRI image was too noisy and affected the selection of neighboring voxels. In order to investigate whether MRI noise level affects the selection of neighboring voxels for smoothing, three sets of PD MRI images were generated by MRiLab with 3 different noise levels: noise-level-0, noise-level-10 and noise-level-30.

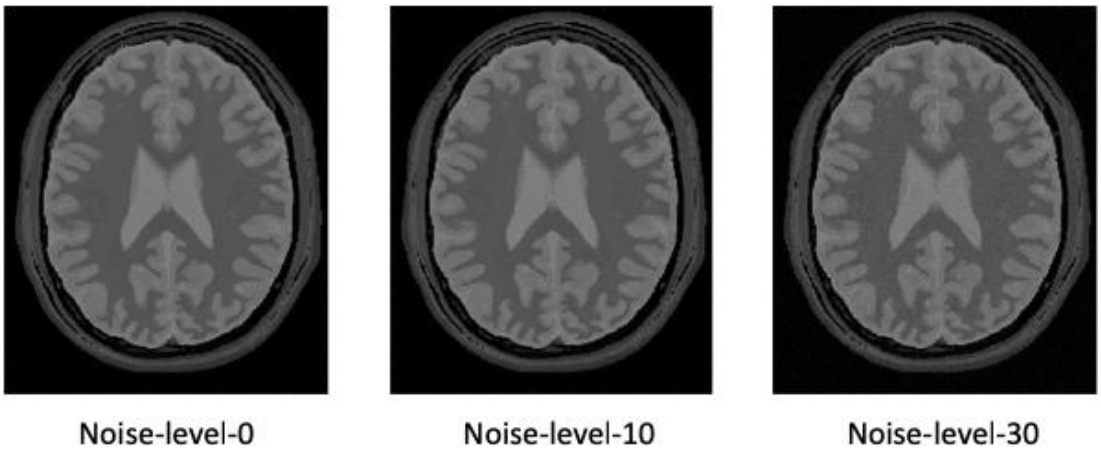

Figure 20: PD-weighted MRI images with 3 different noise level.

Previous MRI images were generated with noise-level-10. To simulate image noise, MRiLab performs a noise adding process to acquired k-space data. A Gaussian

noise with zero mean and user-defined standard deviation is added to the complex signal. Noise-level-0 means no noise is added. Higher the noise level, more noise is added to the acquired k-space data. PET images were reconstructed with 3 different noise level PD-weighted MRI images.

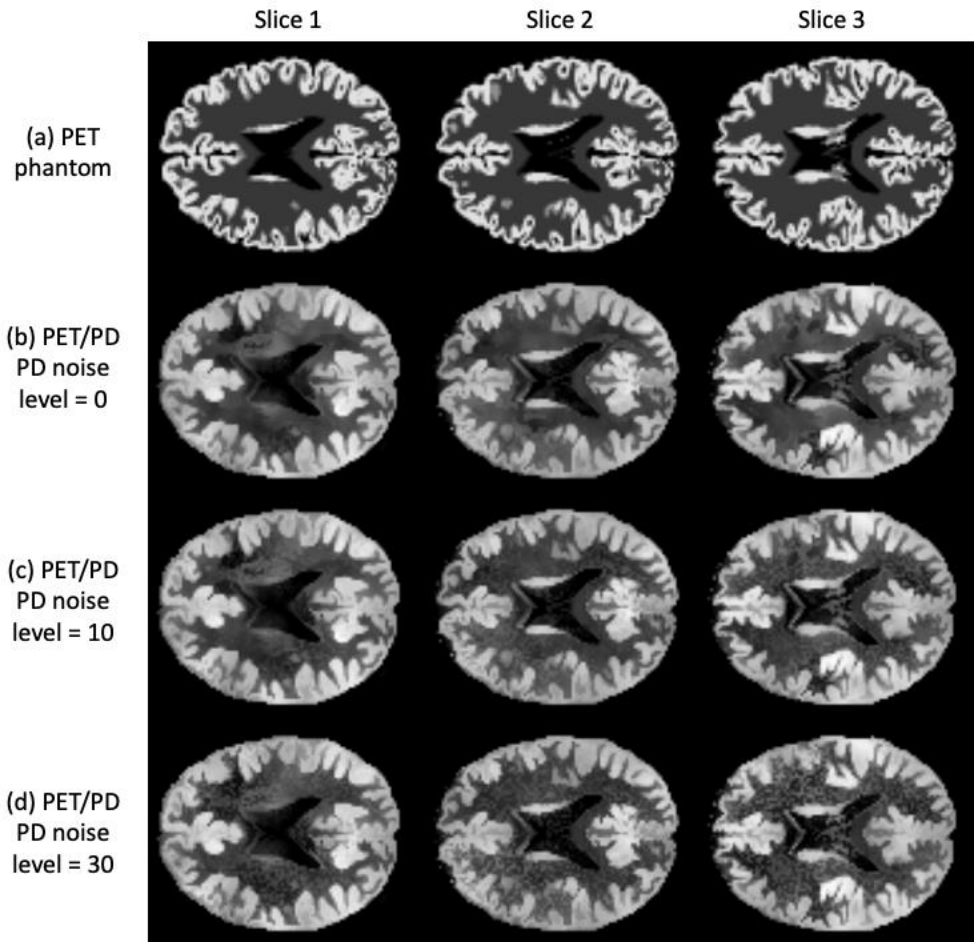

Figure 21: a) PET phantom. (b) PET images reconstructed with noise-level-0, (c) noise-level-10 and (d) noise-level-30 PD MRI images.

The figure above shows that the noise level in PD MRI images doesn't affect the contrast between CSF pockets and surrounding GM tissue in the PET image. Even with MRI noise level 0, the CSF pockets are still not well reconstructed. However, the noise level in the MRI image does affect the reconstructed PET image. As showed in the figure

above, as the noise level in the MRI image increased, the noise level in the PET image also increased, especially in the WM region.

3.8 Highlighted neighboring voxel when implementing different MRI protocols

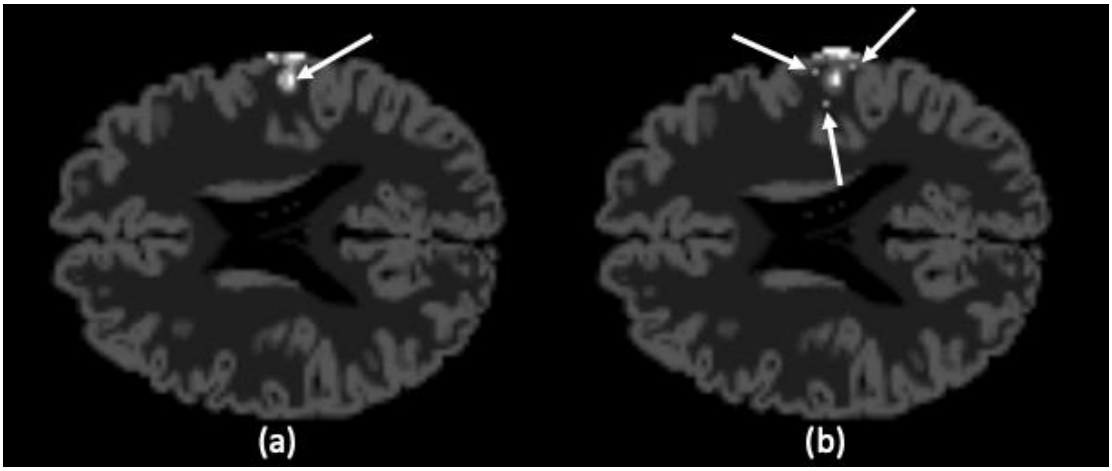

Figure 22: (a) voxels for smoothing when using PD MRI image as prior and (b) voxels selected for smoothing when using ZeroCSF MRI image as prior.

To explain why the CSF pockets and surrounding GM tissue have poor contrast in the PET/PD image, highlighted in Figure 22 are the voxels selected for smoothing with the CSF voxel indicated by the arrow in (a). This voxel of interest is a CSF voxel (ii=56, jj=16, kk=2) which, along with a few other CSF voxels, is surrounded by GM tissue. The number of neighboring voxels selected for smoothing is 20. There are not enough CSF voxels near the voxel of interest and thus some GM or WM voxels must be selected to smooth with the CSF voxel of interest. This is true no matter what the MRI protocol is. In the case of using a PD MRI, GM voxels were chosen. In the case of using the ZeroCSF MRI image as a priori information, some WM voxels, as pointed out by the arrows in Figure-22- (b), were selected to smooth with the CSF voxel of interest.

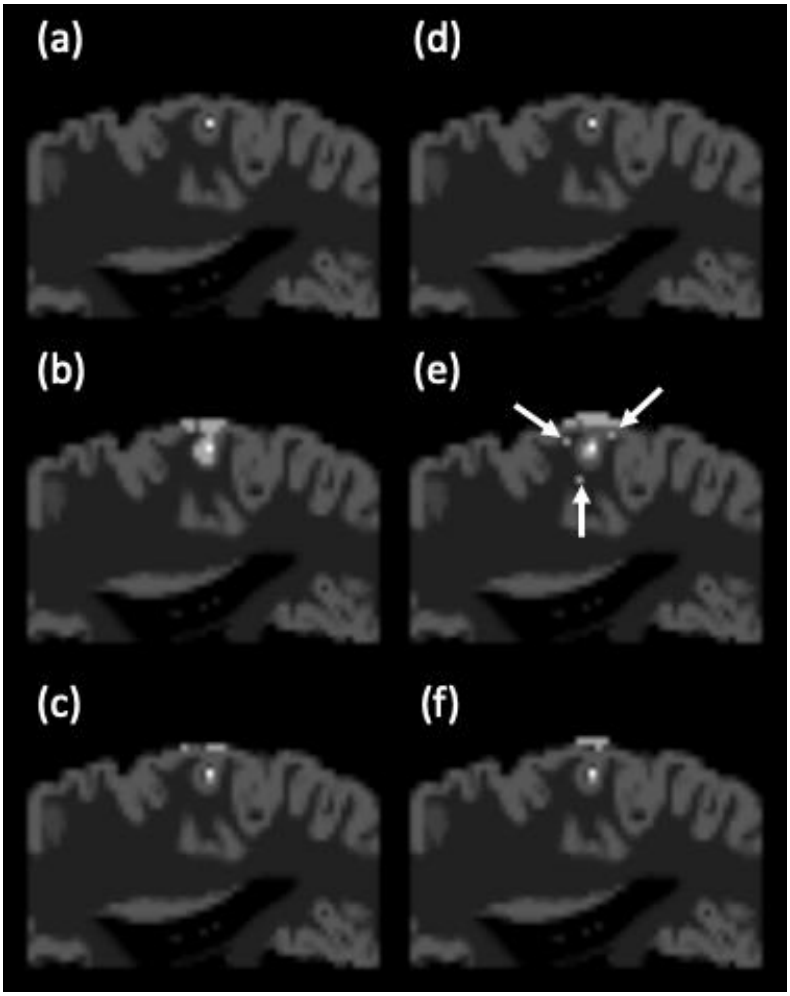

Figure 23: (a) center CSF voxel, (b) primary neighboring voxels and (c) secondary neighboring voxels when using PD prior and (d)-(f) when using ZeroCSF prior.

Since the radiotracer concentration is much higher in the GM (4 $\mu Ci/ml$) than in the WM (1 $\mu Ci/ml$), the CSF voxel of interest tends to have a higher activity when smoothing with GM (which is more likely when using PD MRI image) than when smoothing with WM (which is more likely when using the ZeroCSF MRI image).Tables 5 and 6 provide a list of neighboring voxels selected for smoothing when using ZeroCSF and PD MRI images as a priori information. The mean activity concentration of the selected neighboring voxels in the PET phantom when using ZeroCSF MRI image for the

prior is 1.125 $\mu Ci/ml$, while the mean value of the selected neighboring voxels when using PD MRI image for the prior is 2.25 $\mu Ci/ml$. This is because more GM voxels, which have a true radiotracer concentration of 4 $\mu Ci/ml$, were selected to smooth with the CSF voxel in the case of using PD image as prior. Table 7 gives a list of numbers of neighbors selected in different tissue types. Less CSF voxels and more GM voxels were selected for CSF smoothing when using PD MRI image as prior as compared with when using ZeroCSF MRI image as prior.

Table 5 List of neighboring voxels selected when using ZeroCSF image as prior. ii, jj, kk are the coordinates of the selected voxels.

ii	jj	kk	Phantom value ($\mu Ci/ml$)	Predominant Tissue Type
54	10	2	0	CSF
55	10	2	0	CSF
56	10	2	0	CSF
57	10	2	0	CSF
53	10	2	0	CSF
56	11	2	0	CSF
59	11	2	0.5	CSF/WM
55	11	2	1	WM
55	16	2	0	CSF
51	11	2	2	CSF/GM
54	11	2	2	CSF/GM
55	14	2	2	CSF/GM
57	11	2	2	CSF/GM
58	11	2	2	CSF/GM
54	16	2	2.5	CSF/GM
54	15	2	2	CSF/GM
51	14	2	1	WM
58	13	2	1	WM
53	20	2	1	WM
52	11	2	3.5	CSF/GM

Table 6 List of neighboring voxels selected when using PD image as prior. ii, jj, kk are the coordinates of the selected voxels.

ii	jj	kk	Phantom value ($\mu Ci/ml$)	Predominant Tissue Type
56	11	2	0	CSF
55	11	2	0	CSF
55	16	2	0	CSF
57	11	2	0	CSF
51	11	2	0	CSF
54	11	2	2	CSF/GM
54	15	2	2	CSF/GM
55	14	2	2	CSF/GM
54	16	2	2.5	CSF/GM
55	12	2	3.5	CSF/GM
53	15	2	4	GM
52	12	2	4	GM
52	11	2	3.5	CSF/GM
54	17	2	4	GM
53	16	2	4	GM
54	14	2	4	GM
55	17	2	4	GM
54	12	2	4	GM
56	12	2	3.5	CSF/GM
55	13	2	4	GM

Table 7 List of number of neighbor selected in different tissue type.

MRI protocol	Number of neighbors selected in different tissue				
	CSF	CSF/WM	WM	CSF/GM	GM
PD	5	0	0	7	8
ZeroCSF	7	1	3	8	1

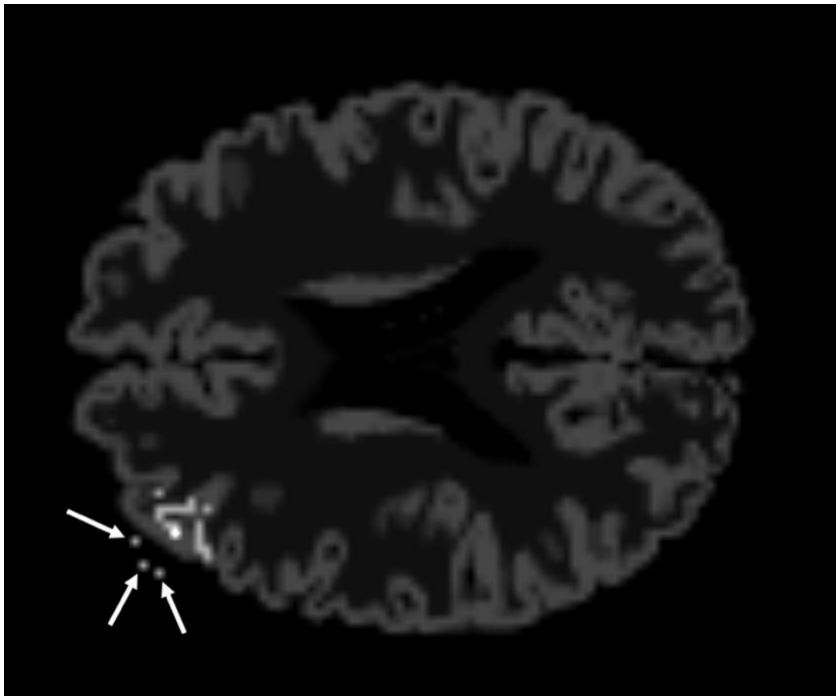

Figure 24: Neighboring voxels selected for smoothing of a GM voxel on the PET phantom when using ZeroGM MRI image as prior.

In the case of using ZeroGM MRI image for a priori information, the neighboring voxels selected for smoothing with a GM voxel of interest (the brightest voxel) are highlighted on the PET phantom. As pointed out by the arrows in Fig.24, three voxels outside the brain were selected for smoothing with the GM voxel. Those three voxels are out of the brain which could be skull or fat tissue voxels. The smoothing interactions between those skull/fat voxels and the GM voxels may cause the washout of the periphery region in the PET/ZeroGM images. The washout phenomenon was not observed in the PET/ZeroWM images. This may be due the skull/fat tissue voxels were relatively far from the WM voxels than were from the GM voxels so there were not selected for the smoothing of WM voxels, even though the skull/fat tissue voxels have similar signal intensities as the WM voxels in the ZeroWM MRI image.

4. Discussion

In this study, different MRI protocols were investigated for their ability to correct for the partial volume effect in PET/SPECT images by using a Bayesian image reconstruction approach (Bowsher et al., 2004). PET images were reconstructed with different MRI images. Compared with OSEM images which did not using any anatomical prior, PET/SPECT images reconstructed with MR images were less blurry and more detail was visible. PET/ZeroCSF had the best-looking image, and it also had the lowest RMSE values at each prior strength. RMSE values were also calculated separately for GM, WM, and CSF. PET/ZeroCSF gave the lowest RMSE value for each tissue type. In order to investigate why the CSF pockets were not visible in PET images reconstructed with T1 and PD images, we proposed two hypotheses: 1. The noise level in the MRI images affected the PET image reconstruction; 2. There were not enough neighboring CSF voxels to smooth with the CSF pockets in GM. To evaluate the first hypothesis, we generated three sets of PD MRI images with different noise levels and kept other parameters the same for the PET image reconstruction. The result showed that changing the noise level in the MRI image didn't strongly affect the contrast between the CSF pockets and surrounding GM tissue. However, as the noise level in the MRI image increased, the noise level in the reconstructed PET image also increased, especially in the WM region.

To evaluate the second hypothesis, we highlighted the neighboring voxels selected to smooth with the CSF pockets and displayed them on the PET phantom (figure 22). We found that some GM voxels (which have a much higher radiotracer

concentration) were selected to smooth with the CSF voxel in case of using the PD prior. As a result, the CSF voxel had a higher value than it actually should have. As a second test, we reduced the number of neighboring voxels selected for the CSF smoothing, and this resulted in greater contrast between CSF pockets and surrounding GM (the CSF pockets became readily visible). The RMSE values for each tissue type were calculated again after reducing the number of neighboring voxels selected for smoothing. The result showed that the PET/PD image then had the lowest RMSE value for CSF and GM while PET/ZeroCSF image still had the lowest RMSE value for WM. This also indicated that the CSF reconstruction when using PD prior was improved after reducing the number of neighboring voxel selected for CSF smoothing.

So why were the neighboring voxels selected for smoothing different when we applied different MRI images? This might due to the differing tissue contrast level in each MRI image. As shown in Table 4, the PD MRI image has a very poor GM-CSF contrast (-0.0601) compared with the WM-CSF contrast (-0.2502). This suggests that CSF-pocket voxels may choose GM voxels, rather than WM voxels, for smoothing interactions. The ZeroCSF MRI image has a relatively good GM-CSF contrast (1.5331), which is slightly better than the WM-CSF contrast (1.4670). This implies that CSF-pocket voxels may choose WM voxels, rather than GM voxels, for smoothing interactions. Because the GM voxels had similar MRI signal intensities with the CSF voxels in PD MRI image, therefore, some GM voxels were selected for CSF smoothing when the PD MRI image was applied to PET image reconstruction. Smoothing a CSF voxel with GM causes more loss of CSF-GM contrast than does smoothing a CSF voxel with WM, since

WM activity (1 $\mu Ci/ml$) is much closer to CSF activity (0 $\mu Ci/ml$) than it is to GM activity (4 $\mu Ci/ml$).

As for the washout in the peripheral region in PET/ZeroGM images, this might due to that some voxels (skull/fat tissue voxels) outside the brain were selected to smooth with GM voxels (Figure.24) since they have similar MRI signal intensity with the GM voxels in the ZeroGM MRI image. This phenomenon was not observed in the PET/ZeroWM images because the WM voxels are relatively far from those voxels therefore they were not selected for the WM voxel smoothing interactions.

There are several limitations of this study: 1, artifacts were not simulated in the MRI images. Artifacts such as magnetic susceptibility and chemical shift in real MRI images could potentially affect the quality of reconstructed PET images. 2, for the inversion recovery MRI images, a long TR (15s) was used, such a long TR is impractical in the clinic. 3, the registration of MRI and PET image was perfect in this study. Since MRI and PET scans are performed separately in clinic, mis-registration between MRI and PET images should be considered. 4, radiotracer was assumed to be uniformly distributed in each tissue type in the PET phantom which may not be true for real patients. 5. Scatter and attenuation effect were not modeled in the PET scan. Scatter and attenuation were not simulated in the PET scan, to compensate for this, noise was added to the projection data by scaling the projection data. 6. The spatial resolution of PET detector was assumed to be spatially invariant. For real PET imaging system, detector spatial resolution is varying spatially. 7, the neighboring voxels selected for smoothing

interactions were selected in 2-D. Select the neighboring voxels in 3-D may give a better result but this could also increase the computation time.

5. Conclusion

The method (Bowsher et al., 2004) is effective in reducing noise and improving contrast. It is effective at PVE correction. It renders visible structures that are not apparent in OSEM images or in images reconstructed by ICD using isotropic non-anatomical priors. The method (Bowsher et al., 2004) can however suffer performance degradation, or even severe washout as in the PET images using ZeroGM MRI images for prior, when, due to similar MRI intensities, voxels with very different radiotracer concentration are chosen for smoothing interactions. The choice of MRI protocol determines which tissue pairs are most likely to be chosen for cross-tissue smoothing interactions. In the present study, we have identified this effect, elucidated its mechanisms, and illustrated it with specific cases. This work provides understanding of artefactual effects that may occur when using the method (Bowsher et al., 2004), and it may be an important step toward developing techniques which avoid or alleviate these artifacts. Studies involving MRI brain tumor images is an important area for future work.

References

Nordberg, A., Rinne, J. O., Kadir, A., & Långström, B. (2010). The use of PET in Alzheimer disease. Nature Reviews Neurology, 6(2), 78–87. https://doi.org/10.1038/nrneurol.2009.217

Vunckx, K., Atre, A., Baete, K., Reilhac, A., Deroose, C. M., Van Laere, K., & Nuyts, J. (2012). Evaluation of Three MRI-Based Anatomical Priors for Quantitative PET Brain Imaging. IEEE Transactions on Medical Imaging, 31(3), 599–612. https://doi.org/10.1109/TMI.2011.2173766

Shin, J., Lee, S.-Y., Kim, S. J., Kim, S.-H., Cho, S.-J., & Kim, Y.-B. (2010). Voxel-based analysis of Alzheimer's disease PET imaging using a triplet of radiotracers: PIB, FDDNP, and FDG. NeuroImage, 52(2), 488–496. https://doi.org/10.1016/j.neuroimage.2010.04.013

Thomas, B. A., Erlandsson, K., Modat, M., Thurfjell, L., Vandenberghe, R., Ourselin, S., & Hutton, B. F. (2011). The importance of appropriate partial volume correction for PET quantification in Alzheimer's disease. European Journal of Nuclear Medicine and Molecular Imaging, 38(6), 1104–1119. https://doi.org/10.1007/s00259-011-1745-9

Frisoni, G. B., Fox, N. C., Jack, C. R., Scheltens, P., & Thompson, P. M. (2010). The clinical use of structural MRI in Alzheimer disease. Nature Reviews Neurology, 6(2), 67–77. https://doi.org/10.1038/nrneurol.2009.215

Johnson, K. A., Fox, N. C., Sperling, R. A., & Klunk, W. E. (2012). Brain Imaging in Alzheimer Disease. Cold Spring Harbor Perspectives in Medicine, 2(4), a006213–a006213. https://doi.org/10.1101/cshperspect.a006213

Bowsher, J. E., Hong Yuan, Hedlund, L. W., Turkington, T. G., Akabani, G., Badea, A., … Johnson, G. A. (2004). Utilizing MRI Information to Estimate F18-FDG Distributions in Rat Flank Tumors. IEEE Symposium Conference Record Nuclear Science 2004., 4, 2488–2492. https://doi.org/10.1109/NSSMIC.2004.1462760

Bettinardi, V., Castiglioni, I., De Bernardi, E., & Gilardi, M. C. (2014). PET quantification: strategies for partial volume correction. Clinical and Translational Imaging, 2(3), 199–218. https://doi.org/10.1007/s40336-014-0066-y

Zaidi, H. (Ed.). (2005). Quantum analysis in nuclear medicine imaging. New York, NY: Springer.

Lange, K., & Carson, R. (n.d.). EM Reconstruction Algorithms for Emission and Transmission Tomography. 12.

Hudson, H. M., & Larkin, R. S. (1994). Accelerated image reconstruction using ordered subsets of projection data. IEEE Transactions on Medical Imaging, 13(4), 601–609. https://doi.org/10.1109/42.363108

Alessio, A., Kinahan, P. PET Image Reconstruction. In Henkin, R. E., Bova, D., Dillehay, G., Karesh, S. M., Halama, J., Wagner, R., & E. Kim, E. (2007). Nuclear Medicine (Vol. 48). https://doi.org/10.2967/jnumed.107.040329

Ahn, S., Ross, S. G., Asma, E., Miao, J., Jin, X., Cheng, L., … Manjeshwar, R. M. (2015). Quantitative comparison of OSEM and penalized likelihood image reconstruction using relative difference penalties for clinical PET. Physics in Medicine and Biology, 60(15), 5733–5751. https://doi.org/10.1088/0031-9155/60/15/5733

Atre, A., Vunckx, K., Baete, K., Reilhac, A., & Nuyts, J. (2009). Evaluation of different MRI-based anatomical priors for PET brain imaging. 2009 IEEE Nuclear Science Symposium Conference Record (NSS/MIC), 2774–2780. https://doi.org/10.1109/NSSMIC.2009.5401952

Bowsher, J. E., DeLong, D. M., Turkington, T. G., & Jaszczak, R. J. (2006). Aligning emission tomography and MRI images by optimizing the emission-tomography image reconstruction objective function. IEEE Transactions on Nuclear Science, 53(3), 1248–1258. https://doi.org/10.1109/TNS.2006.875467

Liu, F., Velikina, J. V., Block, W. F., Kijowski, R., & Samsonov, A. A. (2017). Fast Realistic MRI Simulations Based on Generalized Multi-Pool Exchange Tissue Model. IEEE Transactions on Medical Imaging, 36(2), 527–537. https://doi.org/10.1109/TMI.2016.2620961

Prince, J. L., & Links, J. M. (2015). Medical imaging signals and systems (2nd ed.). Boston: Pearson.

Lipinski, B., Herzog, H., Rota Kops, E., Oberschelp, W., & Muller-Gartner, H. W. (1997). Expectation maximization reconstruction of positron emission tomography images using anatomical magnetic resonance information. IEEE Transactions on Medical Imaging, 16(2), 129–136. https://doi.org/10.1109/42.563658